

## Supporting Information

# Low-spin cyanide complexes of 3-mercaptopropionic acid dioxygenase (MDO) reveal impact of outer sphere SHY motif residues

Nicholas J. York, Molly M. Lockart, Brad S. Pierce\*

Department of Chemistry & Biochemistry, University of Alabama, 250 Hackberry Lane, Tuscaloosa, Alabama 35487, United States

## AUTHOR INFORMATION

### Corresponding Author

\* To whom correspondence should be addressed: Department of Chemistry and Biochemistry, University of Alabama Tuscaloosa, Alabama 35487, USA, Telephone: (205)348-8445. E-mail: [bspiercel@ua.edu](mailto:bspiercel@ua.edu)

## Table of Contents for Supplementary Information

Section	Description	Page
	Analysis of low-spin $d^5$ electronic structure from EPR parameters	2-3
<b>I</b>	UV-vis results for H157N and Y159F $\Delta v$ MDO variants	3
<b>II</b>	$^2\text{H}_2\text{O}$ and $\text{K}^{13}\text{CN}$ EPR studies on complexes <b>1A</b> and <b>1B</b>	3-4
<b>III</b>	EPR experiments with H157N and Y159F $\Delta v$ MDO variants	4-5
<b>IV</b>	ESEEM experiments on ( <b>3MPA</b> /CN)-bound $\Delta v$ MDO (complex <b>1C</b> )	5-6
<b>V</b>	Computational investigation of ( <b>3MPA</b> /CN)-bound H157N $\Delta v$ MDO (complex <b>2C</b> )	7
<b>VI</b>	Computational investigation of ( <b>3MPA</b> /CN)-bound Y159F $\Delta v$ MDO (complex <b>3C</b> )	7-8
<b>VII</b>	Computational investigation of complex <b>1B</b>	8
<b>VIII</b>	TD-DFT Calculations and Results	9
	SI Schemes	10-11
	SI Tables	12-15
	SI Figures	16-23
	Cartesian coordinates for models of <b>1C</b> , <b>2C</b> , and <b>1B</b>	24-31
	References	32

## Analysis of low-spin $d^5$ electronic structure from EPR parameters

Theories for the treatment of EPR results from low-spin  $d^5$  complexes are well established. Using the model initially proposed by Griffith<sup>1</sup> and later developed by Taylor<sup>2</sup>, the relative energies of the  $t_{2g}$   $d$ -orbitals ( $d_{yz}$ ,  $d_{xz}$ , and  $d_{xy}$ ) can be calculated based on  $g$ -values.

$$(3) \quad \begin{aligned} g_z &= 2[(a+b)^2 - c^2] \\ g_y &= 2[(a+c)^2 - b^2] \\ g_x &= 2[a^2 - (b+c)^2] \end{aligned}$$

From these expressions,  $g$ -values can be used to calculate the  $d$ -orbital mixing coefficients using the following expressions:

$$(4) \quad a = \frac{(g_z+g_y)}{D}, \quad b = \frac{(g_z-g_x)}{D}, \quad \text{and } c = \frac{(g_y+g_x)}{D}, \text{ where } D = [8(g_z + g_y - g_x)]^{1/2}$$

Assuming (1) no covalency and (2) a sufficiently large ligand field splitting to prevent orbital mixing of  $t_{2g}$  and  $e_g$  orbitals, then the normalization condition,  $a^2 + b^2 + c^2 = 1$  should hold. Taylor's formulism provides a method to calculate the energy separating the three  $t_{2g}$ -orbitals from the experimental  $g$ -values:

$$(5) \quad \begin{aligned} A &= (E_{yz} - E_{xz})/\lambda = \frac{a+c}{2b} = \frac{g_x}{g_z+g_y} + \frac{g_y}{g_z-g_x} \\ B &= (E_{yz} - E_{xy})/\lambda = \frac{a+b}{2c} = \frac{g_x}{g_z+g_y} + \frac{g_z}{g_y-g_x} \end{aligned}$$

In these expressions, the variable  $\lambda$  represents the one electron spin-orbit coupling parameter. This value typically falls within 400 – 460  $\text{cm}^{-1}$  for low-spin ferric complexes.<sup>3-7</sup> Orbital energies are typically reported in terms of the axial and rhombic distortion from cubic symmetry. Here, the axial splitting ( $\Delta$ ) is defined by the energy difference between the  $d_{xy}$  and the average of the  $d_{xz}$  and  $d_{yz}$  orbitals. The rhombic splitting ( $V$ ) is then defined by the difference in energy between the  $d_{xz}$  and  $d_{yz}$  orbitals. By this convention, the axial and rhombic splitting can be calculated by:

$$(6) \quad \begin{aligned} V/\lambda &= A \\ \Delta/\lambda &= B - (A/2). \end{aligned}$$

Within a frozen, randomly orientated, EPR sample, the alignment and sign of  $g$ -values relative to a  $x,y,z$ -coordinate system cannot be determined *a priori*. Instead,  $g_{\min}$ ,  $g_{\text{mid}}$ , and  $g_{\max}$  are selected from the powder spectrum where  $g_{\min}$  and  $g_{\max}$  represent the largest and smallest numerical  $g$ -values, respectively. In order to align the molecular axis with the  $g$ -tensor, conventions have been adopted largely on the basis of heme metalloproteins such that  $\Delta$  represents the largest distortion along the  $z$ -axis and the smaller rhombic distortion lies within the  $xy$ -plane. Within this “*proper*” coordinate system, the maximum rhombicity ( $V/\Delta$ ) of the system should not exceed 2/3. Selection of a  $g$ -axis system where the rhombic distortion exceeds the axial ( $V/\Delta > 2/3$ ) reflects a rotation of this coordinate system and axes are redefined accordingly. For the systems described here, both the

normalization condition and retention of a “proper” coordinate system ( $V/\Delta < 2/3$ ) was maintained by aligning  $g_{\min}$ ,  $g_{\text{mid}}$ , and  $g_{\max}$  along  $-g_x$ ,  $g_y$ , and  $-g_z$ , respectively.

## I. UV-Vis results for H157N and Y159F *Av*MDO variants

Additions of **3MPA** and cyanide to Fe(III)-*Av*MDO were repeated for the H157N and Y159F variants. Enzyme concentration and stock substrate/cyanide concentrations were prepared as described in the *Materials and Methods* section. As with wild-type enzyme, additions of **3MPA** were performed first to determine the saturating relative concentration. **3MPA** binding to the H157N variant of *Av*MDO was evidenced by a Fe-S LMCT band with a max wavelength of 550 nm. Substrate binding was shown to saturate at 10 molar eq. to enzyme. Cyanide was added to H157N pre-incubated with 10x **3MPA**. Increasing equivalents of cyanide showed a +560  $\text{cm}^{-1}$  blue shift in the maximum wavelength to 670 nm relative to wild-type **1C**, as shown in **Figure S2** (panel A). UV-visible data were fit to a single binding site model (equation S1) to construct the **3MPA** and CN-binding curves presented in **Figure S2** (panels C and D). Fitting parameters are presented in **Table S1**.

$$(S1) \quad [EL] = \frac{\sqrt{(B_{\max}+K_d+[L])-(B_{\max}+K_d+[L])^2-4 \cdot B_{\max} \cdot [L]}}{2}$$

Similar to wild-type *Av*MDO, tight binding was observed for **3MPA** with a  $K_d$  of 0.4 mM. However, cyanide binding to samples prepared from the H157N variant never reached full saturation ( $K_d$  of 3.2 mM).

By comparison to **1C** and **2C**, the UV-visible features for **3C** are more complicated (**Figure S2**). While the absorption maximum (684 nm) is similar, the line width for the (**3C**) Fe-S LMCT band is twice the width exhibited for **1C** and **2C** (~340 versus 170 nm FWHM) (**Figure S2**, panel B). Consequently, the shift in the Fe(III)-S LMCT upon addition of cyanide is less obvious in the Y159F variant. Nevertheless, LMCT bands were produced at 689 nm with increasing addition of **3MPA**. As with wild type and H157N, substrate saturation is obtained at 10 molar eq. **3MPA** relative to enzyme (**Figure S2**, panel B). This  $\lambda_{\max}$  is considerably higher in wavelength compared to wild type and H157N. As for the H157N variant, cyanide binding never fully saturates with a  $K_d$  of 3.4 mM at 684 nm. The  $\lambda_{\max}$  and selected molar extinction coefficients values ( $\epsilon$ ) for wild-type and variant *Av*MDO species is presented in **Table 1**.

## II. $^2\text{H}_2\text{O}$ and $\text{K}^{13}\text{CN}$ EPR studies on complexes **1A** and **1B**

Substitution with  $^2\text{H}_2\text{O}$  buffer is often used to in EPR experiments to identify Fe-bound solvent ligands. There is a near 7-fold decrease in gyromagnetic ratio of  $^2\text{H}$  ( $I = 1$ ) relative to  $^1\text{H}$  ( $I = 1/2$ ) resulting in a significantly lower magnitude of hyperfine splitting. While these are frequently unresolved in CW EPR, samples prepared in  $^2\text{H}_2\text{O}$  will have decreased linewidth relative to  $^1\text{H}_2\text{O}$ . By contrast, the magnetic  $^{13}\text{C}$  ( $I = 1/2$ ) present in samples prepared from  $\text{K}^{13}\text{CN}$  should exhibit a broadening effect due to the interaction of the magnetic nuclei with the paramagnetic metal.

**Table S2** summarizes the  $g$ -values and  $g$ -strain ( $\sigma g$ ) obtained from spectroscopic simulation of low-spin ferric species produced in wild-type and variant Fe(III)-*Av*MDO. As shown in **Figure S3**, samples containing a mixture of **1A** and **1B** were prepared in  $^2\text{H}_2\text{O}$  buffer or using  $\text{K}^{13}\text{CN}$  for comparison to data obtained using natural abundance isotopes. Most notably, species **1A** and **1B** exhibits minor shifts in  $g$ -values ( $\Delta g \sim 0.003$  to 0.008) when prepared in  $^2\text{H}_2\text{O}$  buffer (**Table S3**). For example, the decreased line width for **1A** shown in **Fig. 3A** represents a decrease in the full

width at half-maximum (FWHM) along  $g_2$  of  $\sim 3$  mT. A similar, albeit smaller effect (0.6 mT) is observed for **1B** along the same  $g_2$ -axis. These findings are consistent with  $^1\text{H}/^2\text{H}$  exchange within the first coordination sphere of the Fe(III)-site, suggesting that both **1A** and **1B** are coordinated by at least one water/hydroxide ligand in addition to cyanide.

Both **1A** and **1B** are low-spin Fe(III) species, therefore each must have at least one cyanide ligand. However, only a minor increase in the **1A** line width can be detected samples prepared with  $\text{K}^{13}\text{CN}$ . By contrast, **1B** exhibits significant line broadening along the  $g_2$ -axis as shown in **Figure S3** (*panel B*). By comparison to **1A**, the larger increase in line width for **1B** prepared with  $\text{K}^{13}\text{CN}$  could be attributed to multiple Fe-bound cyanides present on **1B**. This conclusion fits nicely with the observation that **1B** is produced by displacement of **3MPA** from **1C** by excess cyanide. However, this could also be attributed to greater alignment of the **1B**  $g$ -tensor with the molecular axis of the Fe-site. In which case, direct comparison of isotopic effects can be misleading. Consequently, isotopic CW EPR experiments on **1A** and **1B** offer only limited utility with regard to the speciation of CN-bound Fe(III)-*Av*MDO in the absence of substrate.

### III. EPR experiments with H157N and Y159F *Av*MDO variants

Cyanide addition to *Av*MDO was repeated for Fe(III)-H157N and Fe(III)-Y159F variants. As with the wild-type enzyme, the oxidized H157N Fe(III)-*Av*MDO exhibits a high-spin ( $S = 5/2$ ) signal at  $g = 4.3$  consistent with a rhombic ferric iron site ( $E/D \sim 0.33$ ). Treatment of H157N *Av*MDO with a 40-fold molar excess of cyanide results in the formation to two low-spin ferric species with rhombic  $g$ -values (2.48, 2.18, and 1.87) and (2.54, 2.21, and 1.84). To differentiate these from those produced in the wild-type enzyme, H157N CN-bound species are referred to as **2A** and **2B**, respectively. Similar to the wild-type enzyme, the relative distribution of these species is nearly three to one [0.75 eq. **2A** to 0.25 eq. **2B**], albeit **2B** represents the minority fraction for H157N. The  $g$ -values for **2B** are quite similar to wild-type **1B**, with the largest difference being a minor shift along  $g_2$  ( $\Delta g_2 = 0.026$ ) and a slightly increased line width. Negligible changes are observed along  $g_3$  and  $g_1$  ( $\Delta g = 0.005$  and  $0.001$ , respectively). This suggest that the “*B-type*” species [collectively **1B** and **2B**] likely have a similar first Fe-coordination sphere. The **1A** and **2A**  $g$ -values are quite divergent and thus no obvious correlation can be made solely on the basis of EPR data.

Substrate addition to H157N Fe(III)-*Av*MDO showed a similar shift in the ( $S = 5/2$ ) signal as present in the wild-type enzyme suggesting formation of a **3MPA**-bound Fe(III)-*Av*MDO complex (**2S**) analogous to wild-type (**1S**). Addition of cyanide to (**2S**) yields three low-spin ( $S = 1/2$ ) CN-bound species, as shown in **Figure 5**. Two of which are **2A** and **2B**, seen without substrate. The third set of  $g$ -values (2.39, 2.30, and 1.93) is attributed to the (**3MPA**/CN)-bound H157N MDO species, denoted **2C**. The **2C** EPR spectra is similar to wild-type **1C**, but with a shifted  $g_2$  signal. **2A** and **2B** are shown in both low and high relative cyanide concentrations, likely due to binding of as-isolated ferric enzyme which did not bind to substrate.

Much like the wild-type and H157N variant, oxidized Y159F Fe(III)-*Av*MDO shows a  $g \sim 4.3$  signal in EPR diagnostic of high-spin ferric iron. Upon adding cyanide, the  $g = 4.3$  signal attenuates, and multiple cyanide-bound species are shown at  $g = 2$ . Up to this point, EPR spectroscopy reveals only two distinct cyanide binding modes for wild-type *Av*MDO and H157N variant in the absence of substrate. Presumably, each species represents cyanide coordination at a different Fe-site or multiple CN-ligands bound simultaneously. However, cyanide additions made to the Y159F variant of Fe(III)-*Av*MDO results in at least three distinct low-spin rhombic ( $S = 1/2$ )

species with  $g$ -values of (2.33, 2.14, and 1.94), (2.42, 2.20, and 1.90), and (2.47, 2.17, and 1.87). As shown in **Figure 5**, these signals are referred to as **3B**, **3A<sub>1</sub>**, and **3A<sub>2</sub>**, respectively. Species **3B** exhibits the least spread in  $g$ -values ( $g_3 - g_1 = 0.39$ ) and has no obvious analog in either the wild-type or H157N variant. All three  $g$ -values for **3A<sub>1</sub>** exhibit only modest deviations relative to wild-type **1A** ( $\Delta g_3$ ,  $\Delta g_2$ , and  $\Delta g_1 = 0.04$ ,  $-0.03$ , and  $0.01$ ). Similarly, Y159F species **3A<sub>2</sub>** correlates closely with H157N species **2A** with deviations in  $g_1$ ,  $g_2$ , and  $g_3$  of  $-0.01$ ,  $-0.01$ , and  $0.00$ , respectively. Given the structural identity of **1A** and **2A** are unresolved, the implications of seeing similar species in the Y159F variant are limited. Other signals were produced but could not be accurately accounted for by simulation. These are shown near  $g = 2.25$  and  $g = 2.001$ . The signal at  $g = 2.25$  appears to be a derivative signal in accord with a  $g_2$  signal for an anisotropic low spin species. The signal at  $g = 2.001$  is overlapped with a broad signal seen in other samples as well.

No change in the high spin ferric signal was detected upon addition of substrate to the Y159F variant. Based on UV-vis data it is likely that **3MPA**-binding is both low and heterogeneous in nature. Nevertheless, cyanide was added to Y159F saturated with **3MPA**. A single new species, **3C**, was observed in the  $g = 2$  region. The aforementioned low spin cyanide-bound species were also in the sample. Fortunately, **3C** showed  $g$ -values (2.40, 2.26, and 1.92) with little overlap of previous species on the already crowded spectrum. Simulations were able to isolate the (**3MPA**/CN)-bound Y159F species as shown in **Figure 5**. The  $g$ -values are similar to the wild-type counterpart, **1C**, attributed to simultaneous **3MPA** and cyanide binding. Only one new signal was produced when adding cyanide and **3MPA** to Y159F MDO. This agrees well with UV-vis results which showed a LMCT band for the (**3MPA**/CN)-bound species with a line width (126 nm) similar to both wild type and H157N which also only showed one (**3MPA**/CN)-bound species in EPR [**1C** and **2C**].

#### IV. ESEEM experiments on (**3MPA**/CN)-bound *Av*MDO (complex **1C**)

Electron spin echo envelope modulation (ESEEM) experiments were performed to further interrogate the first coordination sphere of **1C**. Samples were prepared in 3 mm quartz tubes with Fe(III)-*Av*MDO concentrations of  $\sim 1$  mM. The relative concentrations of enzyme, substrate, and cyanide were maintained relative to UV-visible and CW EPR measurements.

ESEEM spectra were measured using an ELEXSYS E680 EPR spectrometer (Bruker-Biospin, Billerica, MA) equipped with a Bruker Flexline ER 4118 CF cryostat. ESEEM measurements were made at 5 K at seven magnetic fields spanning the region between  $g_3$  and  $g_2$  ( $g_{\max}$  and  $g_{\text{mid}}$ , respectively). Data were collected using a three pulse stimulated echo sequence,  $\pi/2 - \tau - \pi/2 - T - \pi/2 - \tau + T - \text{echo}$ , where  $\pi/2$  represents a 16 ns microwave pulse, and  $T$  and  $\tau$  represent delays between the pulses. The delay time  $\tau$  was set to 136 ns, and the pulse sequence was repeated at a rate of 0.5 kHz. The fast spin relaxation behavior of **1C** required small values of  $\tau$  and ruled out other experiments such as electron nuclear double resonance (ENDOR) spectroscopy. Spectra were processed using Xepr (Bruker-Biospin, Billerica, MA) and custom scripts in MATLAB (Mathworks, 2020a). In brief, spectra were phased to minimize the imaginary component of the signal before removing the imaginary part. Then, the natural log was taken, and the result was fit to a second-order polynomial, which was then subtracted to remove the background echo decay. A cosine bell apodization function was then applied to the spectra to minimize noise. The result was zero-filled to 1024 points, and the Fourier transform was calculated. The spectra are plotted as the real part of the Fourier transform. Plots were made using OriginPro version 2019 (OriginLab, Northampton MA).

ESEEM is a pulsed EPR technique that directly observes magnetic nuclei that are coupled to the unpaired spin via hyperfine couplings. Consequently, ESEEM measurements can be a useful tool for characterizing metalloenzyme structure.<sup>8,9</sup> In an ESEEM experiment, coupled nuclei are identified by their periodic modulation of the electron spin echo as a function of time.<sup>10-12</sup> Typically, the time domain spectrum is Fourier transformed into a frequency domain spectrum in which peaks from individual nuclei can be identified based on their hyperfine couplings and respective ENDOR frequencies.<sup>13</sup> There are several coupled magnetic nuclei in complex **1C**. **Figure S5** shows the 3-pulse ESEEM spectrum of **1C** at 292 mT, which falls near  $g_3$  ( $g_{\text{max}}$ ) in the EPR spectrum. Peaks below 8 MHz represent coupled  $^{14}\text{N}$  nuclei ( $I = 1$ ) that are close to the low-spin Fe(III) center. These include the coordinated and remote  $^{14}\text{N}$  on each of the three histidine residues, three  $^{14}\text{N}$  on the second-sphere Arg168 residue, and the  $^{14}\text{N}$  on the coordinated cyanide. In general,  $A \sim 2$  MHz hyperfine couplings dominate  $^{14}\text{N}$  ESEEM spectra; the assignment of these peaks depends not only on the hyperfine coupling, but also on the anisotropy of the hyperfine coupling. Each coordinated histidine residue has two  $^{14}\text{N}$  that can contribute to the ESEEM spectrum. Metalloenzymes in which the metal is coordinated by histidine residues typically exhibit large hyperfine couplings for the directly coordinated  $^{14}\text{N}$  on histidine.<sup>14</sup> In fact, in the diiron cluster of the hydroxylase component of methane monooxygenase, the directly coordinated  $^{14}\text{N}$  from histidine residues have hyperfine couplings that are  $\sim 16$  times larger than the remote  $^{14}\text{N}$ .<sup>15,16</sup> The peaks below 8 MHz in the ESEEM spectrum of **1C** appear intense, but  $^{14}\text{N}$  ESEEM has strong orientation dependence, meaning peak intensities fluctuate significantly depending on the position of the nucleus relative to the low-spin Fe(III) center.<sup>14</sup> This obfuscates peak assignment in the case where so many  $^{14}\text{N}$  contribute to the overall spectrum. However, other coupled nuclei can offer insight into the structure of species **1C**. In particular,  $^1\text{H}$  peaks, which are shifted in the frequency domain spectrum from  $^{14}\text{N}$  peaks, can provide additional structural details.

The ESEEM spectrum in **Figure S5** contains a  $^1\text{H}$  ( $I = 1/2$ ) peak at the  $^1\text{H}$  Larmor frequency ( $\sim 12.4$  MHz at this magnetic field). This peak is from  $^1\text{H}$  that are near the Fe center well within 1 nm, namely those on the histidine residues and on **3MPA**. While many of these  $^1\text{H}$  peaks overlap, any exchangeable  $^1\text{H}$  should disappear in deuterated samples, lowering the intensity near the  $^1\text{H}$  peak. Therefore, we examined whether a solvent-based ligand like  $\text{H}_2\text{O}$  or  $\text{OH}^-$  is bound to or near the Fe(III) center. **Figure S6** shows a comparison of  $^1\text{H}/^2\text{H}$  ESEEM spectra taken at magnetic fields spanning the region between  $g_2$  and  $g_3$ . The peaks in the  $^1\text{H}$  region of the spectra ( $\sim 12.4$  MHz) show no significant change. As samples prepared in  $^2\text{H}_2\text{O}$  buffer exhibit no significant loss of peaks within the  $^1\text{H}$  region of the ESEEM spectra, it is unlikely that the low-spin Fe(III) site of **1C** contains a directly coordinated solvent ligand. Having, it is also possible that the intense  $^{14}\text{N}$  modulation originating from three coordinated His residues, CN, and nearby His157 and Arg168 masks detection of coordinated  $^1\text{H}_2\text{O}$ . Consequently, the utility of ESEEM experiments for structural analysis of **1C** is quite limited.

## V. Computational investigation of (3MPA/CN)-bound H157N *Av*MDO (complex 2C)

For the H157N *Av*MDO variant, the conserved SHY motif has been altered, to SNY, allowing for retention of an extended H-bonding network, but without the potential for His-ionization. Assuming an equivalent first-coordination sphere for **1C** and **2C**, the orientation of H-bonding interaction between the outer sphere Tyr159 and (3MPA/CN)-bound Fe-site can be modeled for **2C** following the same procedure described for the wild-type for **1C**. Each model can then be evaluated by comparison of experimental and CASSCF/NEVPT2-calculated *g*-values. However, an additional complication arises when considering the orientation of the asparagine H-bond donation within the H157N variant. As illustrated in **Scheme S1**, the direction of Asn157 H-bond donation can be switched to favor Tyr159 or Ser155 by rotation of the Asn-amide along the C $\beta$ -C $\gamma$ -bond. Therefore, four models were optimized for the H157N variant to account for all possible H-bonding networks.

H157N structural model **M3** is similar to the wild-type model **M2** in that the Tyr-OH donates an H-bond to the Asn-carbonyl group, leaving the Asn-amide to donate an H-bond to Ser155. This leaves the Fe-bound cyanide without an H-bond donation from the SHY motif. Model **M4** retains the same H-bond donation from the Asn-amide to Ser155-O-atom, but switches H-bond donation of Tyr159-OH to the Fe-bound cyanide. Rotation of the Asn-amide along the C $\beta$ -C $\gamma$  bond reverses the orientation of H-bonding within the outer-sphere network. In this instance, H-bond donation from Ser-OH to Asn-carbonyl aligns the Asn-amide for donation to either the Fe-bound cyanide (**M5**) or the O-atom of Tyr159 (**M6**). For both models **M5** and **M6**, Tyr159 H-bond donation to the Fe-bound cyanide is also included.

As with the wild-type **1C** calculations, the CASSCF/NEVPT2 process was repeated for these models (**M3-M6**) using a (11,8) active space and point charges in the place of the outer sphere residues. A comparison between the experimentally observed and CASSCF/NEVPT2-calculated *g*-values for each model is presented in **Table 3**. Here, model **M3** provides a greater agreement with the experimental *g*-values with a near 2-fold decrease in RMSD [0.016 for (**M3**) relative to the next closest match, 0.025 for **M5**]. **Table S6** shows that **M3** also shows the best agreement in *g*-shifts between wild type and H157N as compared to calculated *g*-values of **M1**.

## VI. Computational investigation of (3MPA/CN)-bound Y159F *Av*MDO (complex 3C)

The Y159F variant of *Av*MDO eliminates the possibility for any outer-sphere H-bonding interaction from the tyrosine phenol group. However, the *g*-values for **3C** more closely match **1C** [as opposed to **2C**], suggesting the presence of H-bond donation to the Fe-bound cyanide. As shown in **Table 2**, **3C** exhibits only a minor shift in the diagnostic central *g*-value (*g*<sub>2</sub>) relative to wild-type **1C**. Similarly, the iron-sulfur charge transfer band in the Y159F variant [**3C**, 684 nm] is only blue shifted by 12 nm (~ 3.2 kJ/mol). This creates an apparent dilemma as the phenylalanine replacing tyrosine has no means of donating a hydrogen bond to the Fe-bound cyanide. It is therefore speculated that, in the absence of Tyr159, another active site moiety that contributes a weak H-bond may take its place.

Replacement of Tyr159 with Phe does not substantially increase the size of the active site cavity, therefore it is unlikely that this mutation results in a vast rearrangement of 3MPA-binding at the Fe-site. Instead, the two models presented in **Scheme S2** were deemed reasonable as they both minimally change the overall outer sphere environment while simultaneously donating a hydrogen bond to the Fe-bound cyanide. Model **M7** considers a tautomerized H157 H-bond

donation from the  $\delta$ -N atom with a deprotonated  $\epsilon$ -N. Model **M8** features a solvent water donating an H-bond to both the His157  $\delta$ -N and the axial Fe-bound cyanide. A comparison of experimental and calculated CASSCF/NEVPT2-calculated  $g$ -values for each model is presented in **Table 3**. Model **M8** which includes H-bond donation from H157 to the Fe-bound cyanide shows the greatest agreement with experimental  $g$ -values [RMSD of 0.030]. However, this agreement is much less than observed with wild-type **1C** or H157N **2C**. Consequently, this model should be considered with greater skepticism. Currently, this model represents our best working hypothesis for H-bonding interactions within the Y159F active site.

## VII. Computational investigation of complex **1B**

Two observations offer some guidance into the nature of the **1B** cyano-species. First, in addition to being present in the absence of substrate, **1B** is also produced by treatment of the (3MPA/CN)-bound Fe(III)-AvMDO (complex **1C**) with excess cyanide. Second, the Fe-S LMCT band decreases at excess cyanide concentrations suggesting displacement of the substrate. Therefore, it can be inferred that the Fe-site binds at least two cyanide anions to yield **1B**. This argument is supported by the increased line broadening for samples of **1B** prepared with  $K^{13}CN$  as compared to **1A**. Based on this reasoning, multiple structures (presented in **Scheme S3**) were optimized for both two and three cyanides bound to the Fe-site. Models containing two Fe-bound cyanides were evaluated to determine the most likely identity of the third ligand (water, hydroxide, and chloride). Structural isomers were also investigated to determine the influence of changing specific coordination sites for each ligand. Finally, a five-coordinate structure was also considered. The resulting models were evaluated by comparison of experimental and CASSCF/NEVPT2-calculated  $g$ -values as described previously. Based on this analysis, preliminary results found a 6-coordinate  $(CN)_2$ -bound Fe-site with one unidentified ligand showed best agreement. Of the three models tested, only those including hydroxide as the third (non-cyano ligand) yielded  $g$ -values similar to those experimentally measured. Using hydroxide as the third ligand, multiple arrangements were optimized with hydroxide placed *trans* to each His-residue (His90, His92, or His142) to find the most stable structural isomer. These orientations are shown in **Scheme S4**. The workflow of CASSCF/NEVPT2 calculations of these models is shown in **Table S7**. From this evaluation it was determined that positioning cyanide within the equatorial positions (*trans* to H92 and His142), and coordination of hydroxide in the axial position (*trans* to H90) was most favorable. In this configuration, CASSCF/NEVPT2-calculated  $g$ -values reasonably reproduce experimental values for models with the hydroxide donating an H-bond to the O-atom Try159 phenol group (**Figure S7**), which in turn donates an H-bond to His157. The  $g$ -values were calculated to show very good agreement with an RMSD of 0.013.

Of note, an equivalent  $(CN)_2$ -bound structure can also be modeled for samples prepared from the H157N variant **2B** which account for the shifted central  $g$ -value ( $g_2$ ) relative to wild-type **1B**. Following a similar procedure as outlined for **1B**, CASSCF/NEVPT2-calculated  $g$ -values are in good agreement for **2B** (RMSD: 0.007). Given the similarity between calculated and experimental  $g$ -values obtained for wild-type **1B** and the H157N variant **2B**, this model represents our best working hypothesis for the structure.



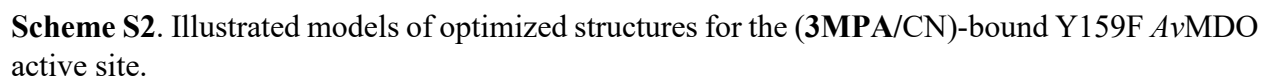
## VIII. TD-DFT Calculations and Results

Single point calculations were performed using time-dependent DFT to elucidate the effect of hydrogen bond donation from Tyr159 to iron-bound cyanide of **1C**. Namely, how the absence of this hydrogen bond would affect the transition energy of the Fe-S LMCT band. A shift in the LMCT band from wild type (696 nm) to the H157N variant (670 nm) was shown for their corresponding (**3MPA/CN**)-bound ferric species (**1C** and **2C**, respectively).

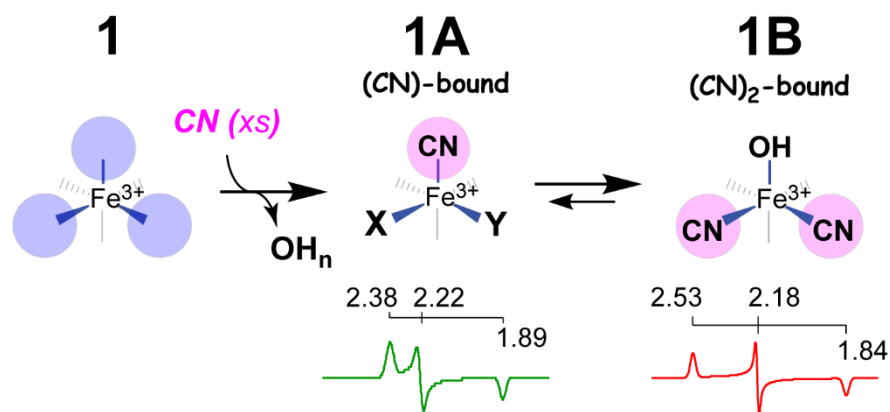
A model for the active site was optimized using the same methods described in the main text with and without Tyr159 donating a hydrogen bond to iron-bound cyanide. For simplicity, residues His157 and Ser155 were excluded from both structures and Tyr179 was excluded from the model without hydrogen bond donation. TD-DFT was performed using the CAM-B3LYP functional with the same basis sets used for the optimization.<sup>1</sup> The Tamm-Dancoff approximation was used to calculate 40 excited states.<sup>2,3</sup> This method has been successfully used to predict optical spectra of  $S \rightarrow Fe$  LMCTs for thiol dioxygenases by Brunold *et al.*<sup>4,5</sup>

**Figure S8** shows the TD-DFT calculated spectra of (**3MPA/CN**)-bound *Av*MDO with and without Tyr159. The absence to the hydrogen bond donating tyrosine residue resulted in a shift of  $570\text{ cm}^{-1}$  (6.79 kJ/mol) in the peaks shown in the  $18,000 - 20,000\text{ cm}^{-1}$  range. An electron density difference map (EDDM) is also shown in **Figure S8** for the most intense transition in the model with Tyr159. The negative density in the sulfur p-orbital and positive density in the iron d-orbital confirms this peak was calculated as a LMCT. The shift in energy is also observed experimentally at 6.7 kJ/mol, giving strong corroboration of the shift in the LMCT band between species **1C** and **2C** being due to a shift in hydrogen bonding orientation by Tyr159.

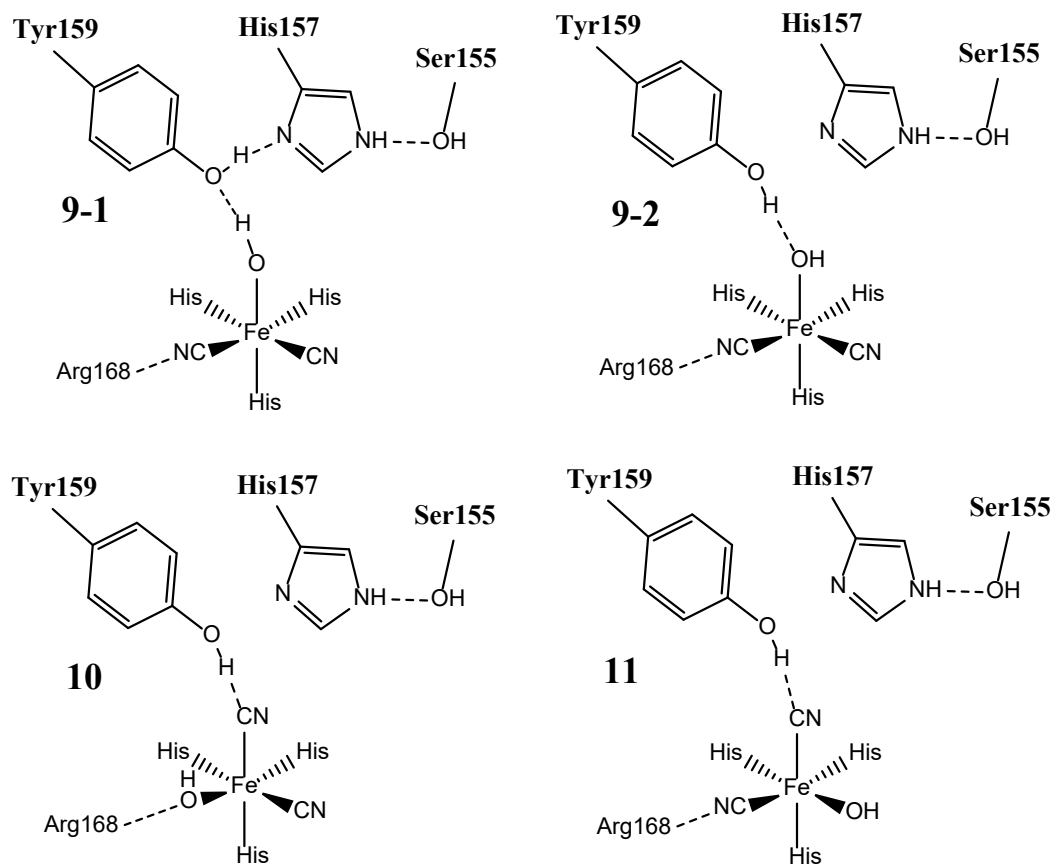
**Scheme S1.** Illustrated models of optimized structures for the (3MPA/CN)-bound H157N AvMDO active site.



**Scheme S3.** Summary of speciation produced by addition of cyanide to Fe(III)-AvMDO.



**Scheme S4.** Illustrated models of species **1B** of optimized structures for the cyanide-bound wild-type AvMDO active site.



## TABLES.

**Table S1.** Fitted binding parameters for **3MPA** to ferric enzyme (wild type, H157N and Y159F) and cyanide to each **3MPA**-bound complex. Also included are the  $\lambda_{\max}$  for each LMCT band and calculated extinction coefficients for wild-type species.

	$K_d$ (mM)	E:L /E <sub>T</sub>	R <sup>2</sup>	$\lambda_{\max}$ (nm)	$\epsilon$ (M <sup>-1</sup> cm <sup>-1</sup> )
WT + <b>3MPA</b>	0.5 ± 0.1	1.00	0.948	584	2965
H157N+ <b>3MPA</b>	0.4 ± 0.1	0.41	0.965	550	-
Y159F + <b>3MPA</b>	0.7 ± 0.2	0.10	0.971	689	-
WT- <b>3MPA</b> + CN	2.3 ± 0.3	0.55	0.995	696	1803
H157N- <b>3MPA</b> + CN	3.2 ± 0.2	0.40	0.995	670	-
Y159F- <b>3MPA</b> + CN	3.4 ± 0.5	0.10	0.981	684	-

**Table S2.** Simulated EPR parameters for low spin ferric AvMDO species.

Sample+CN	Species	$g_3$	$g_2$	$g_1$	$\sigma g_3$	$\sigma g_2$	$\sigma g_1$	$\Delta g$	Rg
AvMDO	<b>1A</b>	2.382	2.226	1.892	0.018	0.011	0.010	0.49	0.64
	<b>1B</b>	2.531	2.188	1.843	0.014	0.002	0.008	0.69	1.00
AvMDO+ <b>3MPA</b>	<b>1C</b>	2.394	2.240	1.928	0.017	0.005	0.007	0.47	0.66
H157N	<b>2A</b>	2.476	2.180	1.873	0.018	0.001	0.008	0.60	0.98
	<b>2B</b>	2.536	2.214	1.844	0.012	0.016	0.006	0.69	0.93
H157N+ <b>3MPA</b>	<b>2C</b>	2.394	2.295	1.932	0.027	0.010	0.010	0.46	0.43
Y159F	<b>3A<sub>1</sub></b>	2.422	2.198	1.896	0.019	0.002	0.004	0.53	0.85
	<b>3A<sub>2</sub></b>	2.469	2.172	1.874	0.010	0.006	0.006	0.60	1.00
	<b>3B</b>	2.333	2.143	1.942	0.013	0.003	0.004	0.39	0.97
Y159F+ <b>3MPA</b>	<b>3C</b>	2.399	2.259	1.919	0.017	0.005	0.005	0.48	0.58

The total span in  $g$ -values ( $\Delta g$ ) was determined from subtracting the minimum numerical  $g$ -value from the maximum ( $g_3 - g_1$ ). The  $g$ -value rhombicity (Rg) was calculated using the procedure described previously by Fielder *et al.* where  $Rg = 1 - (|g_3 + g_1 - 2g_2|)/\Delta g$ .<sup>3</sup> Within this framework, values of Rg range from 0 (fully axial) to 1 (fully rhombic).

**Table S3.** Simulated EPR parameters of cyano-bound low spin ferric wild-type AvMDO species with  $^{13}\text{CN}$ ,  $^2\text{H}_2\text{O}$ , and natural abundance isotope conditions.

Species	Isotope	$g_3$	$g_2$	$g_1$	$\sigma g_3$	$\sigma g_2$	$\sigma g_1$
<b>1A</b>	-	2.382	2.226	1.892	0.018	0.011	0.010
	$^{13}\text{CN}$	2.382	2.228	1.895	0.019	0.011	0.009
	$\text{D}_2\text{O}$	2.376	2.231	1.897	0.013	0.010	0.006
<b>1B</b>	-	2.531	2.188	1.843	0.014	0.002	0.008
	$^{13}\text{CN}$	2.528	2.187	1.845	0.018	0.006	0.010
	$\text{D}_2\text{O}$	2.523	2.188	1.849	0.014	0.003	0.008
<b>1C</b>	-	2.394	2.240	1.928	0.017	0.005	0.007
	$^{13}\text{CN}$	2.398	2.242	1.927	0.019	0.005	0.008
	$\text{D}_2\text{O}$	2.387	2.241	1.927	0.018	0.008	0.001

**Table S4.** Selected geometric parameters of optimized structures for species **1C** compared to similar (substrate/CN)-bound structures from literature.

	Distance (Å)				Angle (°)			
Species	Fe-S	Fe-O/N <sup>a</sup>	Fe-CN	Fe-N <sub>his</sub> (ave)	Fe-C-N	S-Fe-O/N <sup>a</sup>	C-Fe-His <sub>(trans)</sub>	Ref
<i>Fe(III)-AvMDO</i>								
<b>1C</b> (first-coordination only)	2.14	2.03	1.87	2.15	178.7	97.5	173.3	here
<b>1C</b> (M1) <sup>b</sup>	2.14	2.20	1.86	2.09	178.1	95.3	172.8	
<b>1C</b> (M2) <sup>b</sup>	2.14	2.25	1.89	2.06	172.9	97.8	173.3	
<i>Fe(III)-MmCDO</i>								
CYS/CN-WT (α)	2.28	2.08	1.95	2.07	169.2	86.4	168.6	4, 17
CYS/CN-WT (β)	2.26	2.11	1.95	2.05	176.3	86.1	172.6	4, 17
<i>[Fe<sup>III</sup>(L)(Ph<sub>2</sub>TIP)]BPh<sub>4</sub></i>								
<b>1<sup>ox</sup></b> -CN; L = CysOEt	2.18	2.05	1.91	2.17	176.3	86.8	173.6	17
<b>2<sup>ox</sup></b> -CN; L = 2-MTS	2.20	1.96	1.90	2.17	175.8	90.7	172.3	17

<sup>a</sup> Refers to the substrate O/N-atom coordinated *trans* to His140 (*MmCDO*) or His142 (*AvMDO*). <sup>b</sup> Denotes the direction of hydrogen bond donation from the Tyr159 phenol moiety. The structures for models **M1** (Tyr159 → CN) and **M2** (Tyr159 → His157) are presented in **Figure 7**.

**Table S5.** Calculated  $g$ -values of Models 1 and 2 for the structural determination of  $S = 1/2$  species **1C**. Effects of orbital active space, basis set, and outer sphere point charges are shown.

Model		$g_3$	$g_2$	$g_1$	RMSD
<b>1C</b>	EXP	2.397	2.241	1.928	-
<b>M1</b>	(5,5) gas phase	2.428	2.323	1.929	0.051
	(5,5) SHY (Tyr-OH $\rightarrow$ CN)	2.419	2.288	1.939	0.031
	(11,8) gas phase	2.412	2.303	1.926	0.037
	(11,8) SHY (Tyr-OH $\rightarrow$ CN)	2.372	2.255	1.941	0.019
TZVP	(11,8) SHY (Tyr-OH $\rightarrow$ CN)	2.371	2.248	1.944	0.018
	(11,13) gas phase	2.266	2.196	1.963	0.082
	(11,13) SHY (Tyr-OH $\rightarrow$ CN))	2.250	2.166	1.952	0.096
TZVP	(11,13) SHY (Tyr-OH $\rightarrow$ CN))	2.248	2.164	1.949	0.097
<b>M2</b>	(5,5) gas phase	2.451	2.369	1.921	0.081
	(5,5) SHY (Tyr-OH $\rightarrow$ His157)	2.446	2.370	1.923	0.080
	(11,8) gas phase	2.426	2.312	1.922	0.044
	(11,8) SHY (Tyr-OH $\rightarrow$ His157)	2.399	2.299	1.932	0.034
TZVP	(11,8) SHY (Tyr-OH $\rightarrow$ His157)	2.408	2.298	1.932	0.033
	(11,13) gas phase	2.281	2.200	1.971	0.075
	(11,13) SHY (Tyr-OH $\rightarrow$ His157))	2.266	2.196	1.975	0.084
TZVP	(11,13) SHY (Tyr-OH $\rightarrow$ His157))	2.267	2.197	1.973	0.084

**Table S6:** The experimental difference in  $g$ -values between wild-type species **1C** and H157N species **2C** as compared to calculated differences of modeled complexes calculated by CASSCF/NEVPT2 methods.

Model	$g_3$	$g_2$	$g_1$	RMSD
exp	-0.0033	0.0545	0.0040	-
<b>M3</b>	0.000	0.032	-0.004	0.014
<b>M4</b>	-0.010	0.001	0.004	0.031
<b>M5</b>	0.003	0.011	0.004	0.025
<b>M6</b>	-0.021	0.015	-0.006	0.026

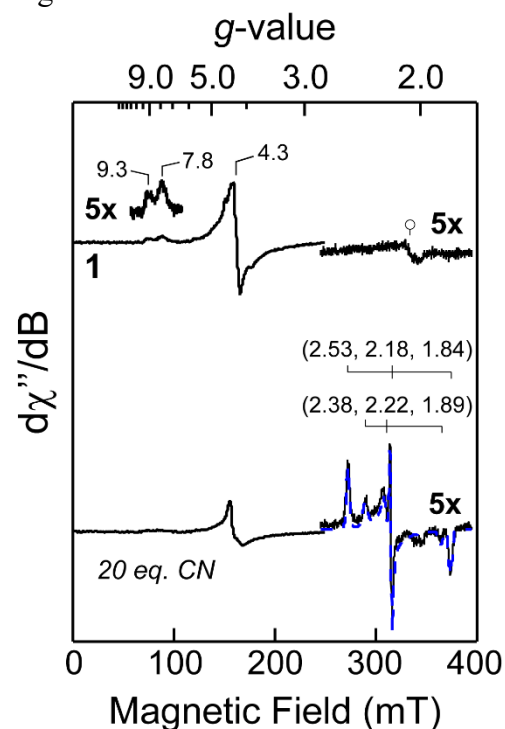
**Table S7.** Workflow of CASSCF/NEVPT2 calculated *g*-values for identification of species **1B**. The flow for each species depicts the addition of Arg168 point charges, followed by the point charges of the SHY motif. This was followed by optimization of the active space orbitals, going from a (5,5) minimal active space to a (9,7) active space with ligand orbitals, to a (9,12) active space with additional *d*-orbitals. Calculations were performed with the def2-SVP basis set except where noted with TZVP.

Model		<i>g</i> <sub>3</sub>	<i>g</i> <sub>2</sub>	<i>g</i> <sub>1</sub>	RMSD
<b>1B</b>	EXP	2.531	2.188	1.843	-
<b>9</b>	(5,5) gas phase	2.466	2.261	1.887	0.062
(9-1)	(5,5) SHY (OH→Tyr-OH→His157)	2.448	2.228	1.868	0.055
(9-1)	(9,7) SHY (OH→Tyr-OH→His157)	2.525	2.236	1.855	0.029
(9-1)	(9,12) SHY (OH→Tyr-OH→His157)	2.508	2.198	1.856	0.016
(9-1) TZVP	(9,12) SHY (OH→Tyr-OH→His157)	2.548	2.201	1.838	0.013
(9-2)	(5,5) SHY (Tyr-OH→OH)	2.519	2.260	1.873	0.046
(9-2)	(9,7) SHY (Tyr-OH→OH)	2.583	2.271	1.861	0.057
(9-2)	(9,12) SHY (Tyr-OH→OH)	2.549	2.220	1.870	0.026
(9-2) TZVP	(9,12) SHY (Tyr-OH→OH)	2.591	2.224	1.853	0.041
<b>10</b>	(5,5) gas phase	2.406	2.232	1.896	0.082
	(5,5) SHY (Tyr-OH→CN)	2.465	2.252	1.871	0.055
	(9,7) SHY (Tyr-OH→CN)	2.512	2.256	1.869	0.044
	(9,12) SHY (Tyr-OH→CN)	2.485	2.219	1.881	0.039
TZVP	(9,12) SHY (Tyr-OH→CN)	2.522	2.235	1.862	0.030
<b>11</b>	(5,5) gas phase	2.418	2.211	1.909	0.076
	(5,5) SHY (Tyr-OH→CN)	2.389	2.188	1.926	0.095
	(9,7) SHY (Tyr-OH→CN)	2.442	2.198	1.922	0.069
	(9,12) SHY (Tyr-OH→CN)	2.430	2.186	1.912	0.070
TZVP	(9,12) SHY (Tyr-OH→CN)	2.459	2.197	1.897	0.052
H157N	EXP	2.536	2.214	1.844	-
H157N TZVP	(9,12) SNY (OH→Tyr-OH→Asn157)	2.545	2.206	1.843	0.007

<sup>a</sup> SHY refers to the inclusion of point charges from the Ser155, His157, and Tyr159 residues.

## FIGURES

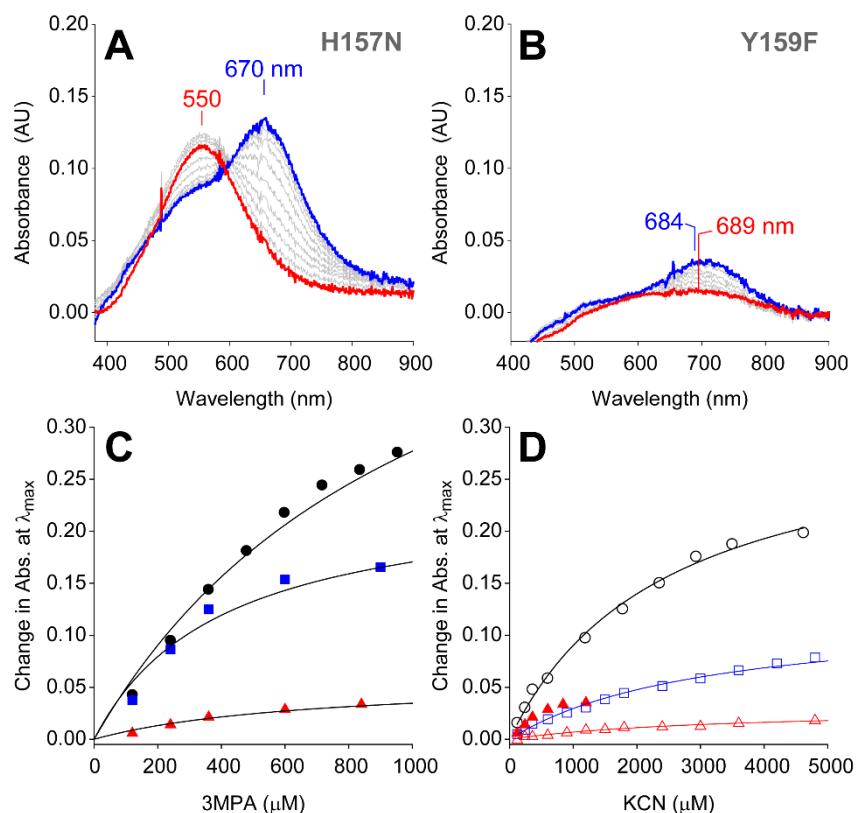
Figure S1



**Figure S1.** Comparison of EPR spectra of Fe(III)-AvMDO (complex **1**) before and after addition of a 20-fold molar excess of KCN. The broad resonance near  $g \sim 2.0$  ( $\circ$ ) is an impurity within the EPR cavity and can be ignored. The two component simulation (*dashed line*) for cyano-bound Fe(III)-AvMDO species is overlaid on the data. Instrumental conditions: microwave frequency, 9.64 GHz, microwave power, 40  $\mu$ W; modulation amplitude, 0.9 mT; temperature, 10 K. Simulation parameters for **1A** and **1B** [Shown in **Figure 1**] are provided in **Table 2**.

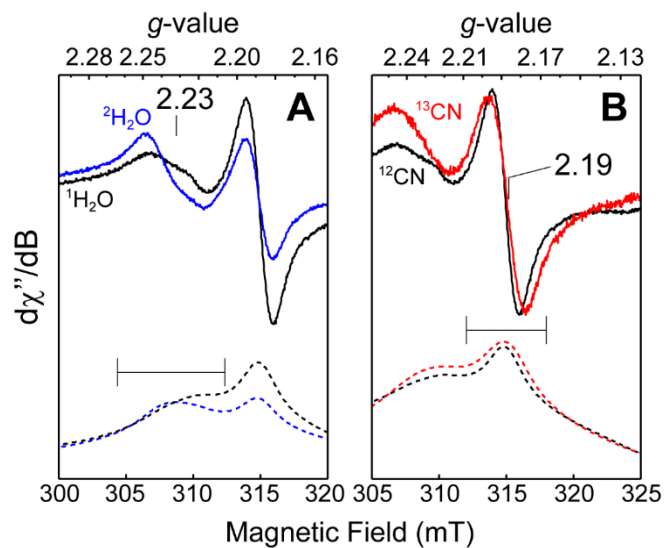


Figure S2



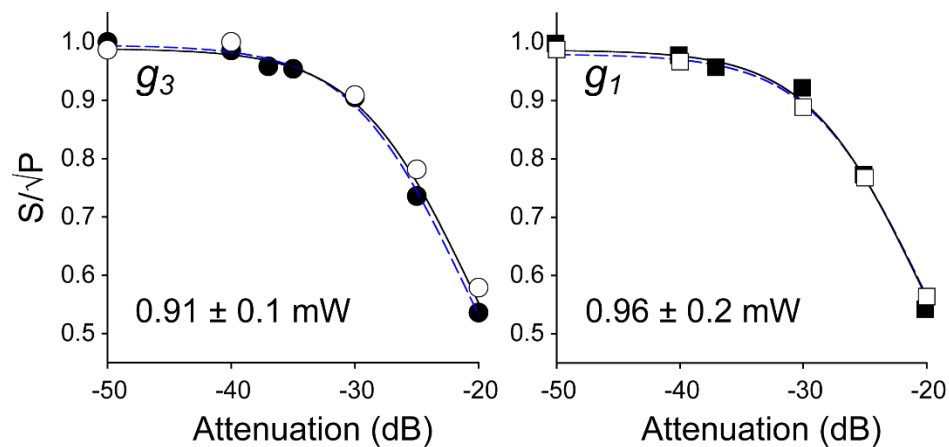
**Figure S2.** Panel A presents the UV-visible spectra of Fe(III)-H157N with **3MPA** (red) followed by addition of cyanide (blue). Panel B presents the UV-vis spectra of Fe(III)-Y159F with **3MPA** (red) followed by addition of cyanide (blue). For clarity, Fe(III)-H157N and Fe(III)-Y159F solutions were blanked before addition of **3MPA** and KCN. Panel C shows the change in absorbance upon treatment of each ferric enzyme with increasing concentration of **3MPA**. Marker shapes used in Panel C and D reflect wild-type *AvMDO* (circle), H157N (square), and Y159F (triangle). Panel D illustrates the change in absorbance upon titration of each (**3MPA**)-bound *AvMDO* with increasing concentration of KCN.

Figure S3



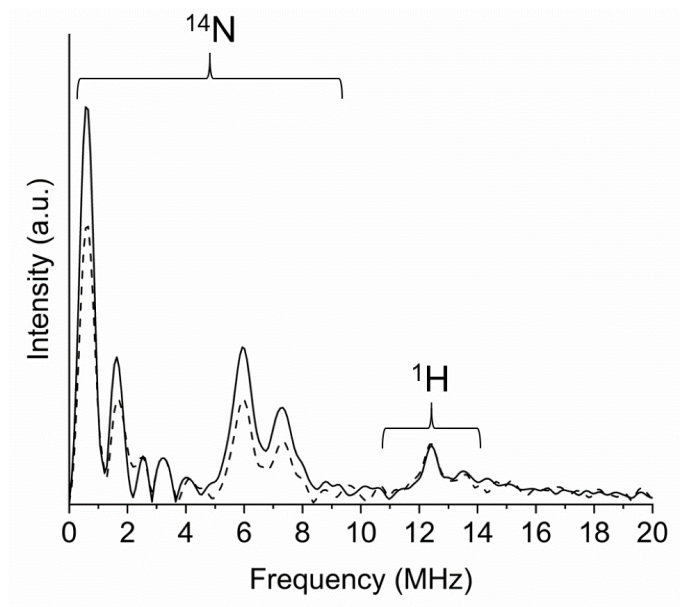
**Figure S3.** EPR spectra of wild-type *AvMDO* with 40x  $\text{K}^{12}\text{CN}$  compared to addition of  $^2\text{H}_2\text{O}$  buffer (*blue*) and  $\text{K}^{13}\text{CN}$  (*red*). The relative concentrations of species **1A** and **1B** are inconsistent through each sample. Therefore, the spectra are scaled to match intensity for comparison of individual *g*-values. Integrated spectra are presented below data (*dashed lines*) to highlight changes upon isotopic substitution.

Figure S4



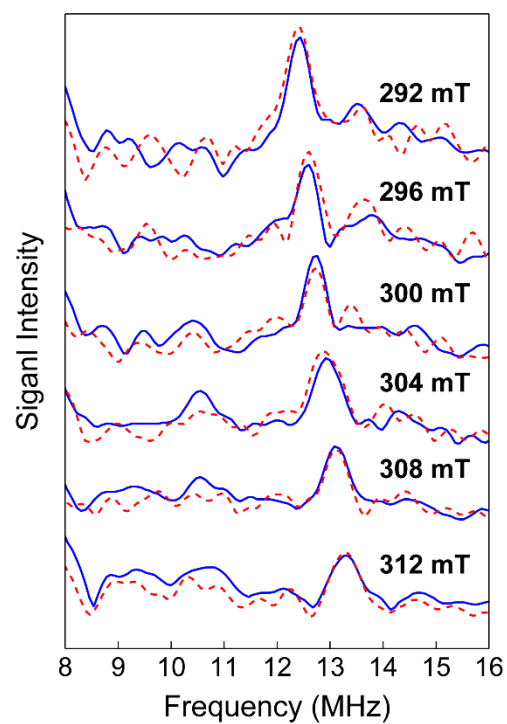
**Figure S4.** Microwave power saturation behavior of **1B** at  $g_3$  (2.53, *circle*) and  $g_1$  (1.84, *square*) in the presence (black points, *solid line*) and absence (white points, *dashed line*) of **3MPA**. For all measurements, a single scan was recorded at 10 K using identical instrumental parameters [microwave frequency, 9.64 GHz, modulation amplitude, 0.9 mT; field width, 150 mT, and sweep time, 184 sec]. The error associated with reported  $P_{1/2}$ -values was estimated from the noise present in the EPR spectrum obtained at lowest power; the marker size is scaled to reflect this value.

Figure S5



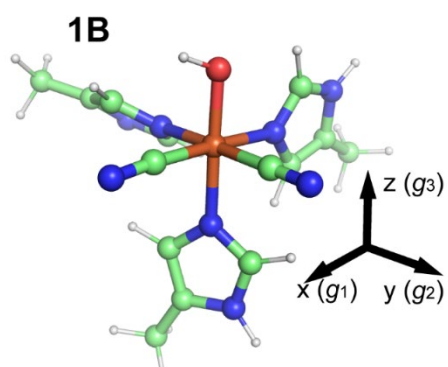
**Figure S5.** 3-pulse ESEEM spectrum of the (3MPA/CN)-Fe(III)-AvMDO (complex **1C**) prepared in  $^1\text{H}_2\text{O}$  (*solid lines*) versus  $^2\text{H}_2\text{O}$  (*dashed lines*). Instrument parameters: microwave frequency, 9.78 GHz; field position of 292 mT; temperature, 5 K; pulse repetition rate, 0.5 kHz;  $\tau$ , 136 ns.

Figure S6



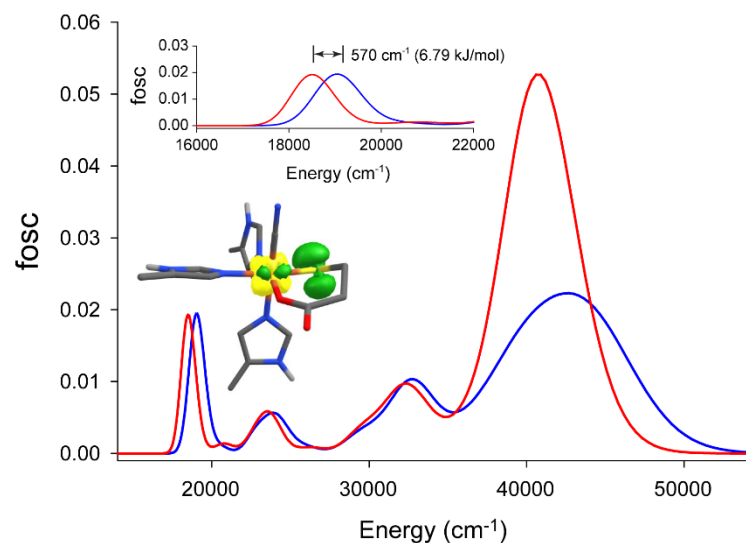
**Figure S6.** Comparison of 3-pulse ESEEM spectra of (**3MPA/CN**)-Fe(III)-AvMDO (complex **1C**) prepared in  $^1\text{H}_2\text{O}$  (solid blue lines) versus  $^2\text{H}_2\text{O}$  (dashed red lines) at magnetic fields spanning the region between  $g_2$  and  $g_3$  in the EPR spectrum.

Figure S7



**Figure S7.** Structural model for **1B** based on best agreement between experimental and CASSCF/NEVPT2 calculated  $g$ -values. Arrows indicated the orientation of the  $g$ -tensor.

Figure S8



**Figure S8.** TD-DFT calculated electronic spectra (*red line*) for optimized model of the (3MPA/CN)-bound Fe(III)-MDO site in which Tyr159 donates an H-bond to the axial Fe-bond cyanide. Calculations performed in the absence of Tyr159 (*blue line*) predict this same transition at 524 nm. (3MPA/CN)-Fe(III) site in the presence of Tyr159 H-bond donation. For comparison, a focused scaling of the calculated Fe-S LMCT charge transfer region is presented as an inset. The electron density difference map (EDDM) illustrates the most intense transition within the calculated Fe-S LMCT band. The negative density (*green*) shown on the S-atom p-orbital and positive electron density (*yellow*) on the *d*-orbital of iron confirms this peak was calculated as a LMCT.

# CARTESIAN COORDINATES (Å) FOR SELECTED MODELS [1C, 2C, and 3C]

## 1C

H	-0.490011	5.029311	-3.581021
C	0.204352	4.224522	-3.906497
C	0.545533	3.281039	-2.800701
C	-0.230060	2.372425	-2.094648
N	1.824610	3.120664	-2.293555
C	1.806216	2.155085	-1.333833
N	0.567089	1.685738	-1.194899
H	1.109289	4.709636	-4.323732
H	-0.295403	3.681169	-4.731834
H	-1.299650	2.170998	-2.183291
H	2.654437	3.636469	-2.595867
H	2.679432	1.810551	-0.772494
H	-4.986142	-0.339433	-3.720921
C	-4.967191	-0.886284	-2.753664
C	-3.888524	-0.365065	-1.866334
C	-2.582895	-0.762913	-1.617458
N	-4.058814	0.791140	-1.115375
C	-2.904598	1.066227	-0.452464
N	-1.990548	0.144310	-0.753131
H	-4.848843	-1.960742	-2.993003
H	-5.960916	-0.755670	-2.279361
H	-2.032050	-1.632344	-1.984149
H	-4.920941	1.338096	-1.054087
H	-2.765366	1.914986	0.222918
H	-1.401658	5.105791	2.540014
C	-1.574793	4.299121	3.276999
C	-1.183946	2.967930	2.730395
C	-0.686840	2.565247	1.499454
N	-1.304354	1.799651	3.467735
C	-0.906372	0.745714	2.710291
N	-0.531074	1.181924	1.504209
H	-2.650720	4.312613	3.553122
H	-0.997056	4.549083	4.190646
H	-0.434340	3.167509	0.624176
H	-1.638467	1.733959	4.431924
H	-0.903273	-0.296192	3.039619
H	7.229434	-6.654706	5.619539
C	6.147789	-6.880824	5.501169
H	5.995384	-7.291479	4.481622
C	5.325967	-5.623883	5.758924
O	5.674656	-4.533938	4.892486
H	5.893683	-7.674588	6.234445



H	5.431627	-5.310107	6.823951
H	4.246692	-5.808446	5.579935
H	6.638494	-4.385241	4.950722
H	2.000883	-8.537079	2.158634
C	1.050385	-8.025844	1.897784
H	0.446311	-8.741008	1.302850
C	1.305080	-6.725436	1.115350
C	2.090641	-5.713519	1.900512
C	3.458776	-5.696862	2.168314
N	1.478008	-4.668701	2.575339
C	2.450564	-4.040663	3.233912
N	3.669768	-4.621131	3.011029
H	0.507659	-7.827050	2.845138
H	0.343794	-6.258879	0.828499
H	1.831120	-6.959552	0.165617
H	4.278128	-6.348371	1.845415
H	2.331743	-3.154756	3.871859
H	4.552432	-4.422047	3.526226
H	-3.788147	-8.886032	-1.413702
C	-4.478632	-8.195719	-1.943014
H	-5.271235	-8.811068	-2.418095
C	-3.771271	-7.351499	-3.016942
C	-2.699789	-6.440022	-2.461462
C	-3.043303	-5.361031	-1.617974
C	-1.329311	-6.662904	-2.712556
C	-2.065724	-4.558146	-1.017058
C	-0.335177	-5.866477	-2.125164
C	-0.694990	-4.822716	-1.247220
O	0.289992	-4.120750	-0.636063
H	-4.963085	-7.560733	-1.171593
H	-4.538227	-6.744541	-3.548576
H	-3.324755	-8.022601	-3.781351
H	-4.106261	-5.151171	-1.410350
H	-1.031858	-7.494523	-3.372616
H	-2.344510	-3.736171	-0.341604
H	0.732257	-6.057640	-2.310830
H	-0.112581	-3.574828	0.093376
H	-4.456839	1.638899	-10.450878
C	-4.274598	2.335005	-9.605166
H	-3.439334	3.005076	-9.900731
C	-4.020066	1.668375	-8.240962
C	-2.770334	0.783833	-8.099286
C	-2.536384	0.388153	-6.630599
N	-1.488307	-0.621029	-6.502167
C	-0.784601	-0.916900	-5.380952

N	-0.898406	-0.160771	-4.266422
N	0.068233	-1.942988	-5.374046
H	-5.181401	2.962357	-9.487776
H	-4.911044	1.064576	-7.957340
H	-3.958172	2.477974	-7.478943
H	-1.869019	1.310108	-8.482724
H	-2.886305	-0.136402	-8.714539
H	-3.491265	0.016654	-6.188274
H	-2.238017	1.289482	-6.053127
H	-1.427173	-1.306674	-7.258679
H	-0.409143	-0.470694	-3.398814
H	-1.714549	0.435822	-4.140632
H	0.245900	-2.459623	-6.235491
H	0.636079	-2.158517	-4.491486
Fe	0.000000	0.000000	0.000000
C	1.465744	-1.881571	-2.104638
O	0.446779	-1.145870	-1.819567
C	2.641794	-2.086923	-1.153830
O	1.593703	-2.407225	-3.243136
C	2.465482	-1.934397	0.352668
S	1.930013	-0.280604	0.890189
H	3.024560	-3.104885	-1.364438
H	3.440466	-2.109683	0.851714
H	1.761024	-2.680020	0.767402
H	3.426477	-1.382890	-1.510020
C	-0.605583	-1.538075	0.845848
N	-1.015257	-2.519276	1.352280

## 2C

H	-0.480691	5.024876	-3.557086
C	0.213672	4.220087	-3.882562
C	0.538982	3.291745	-2.762880
C	-0.178555	2.244604	-2.204788
N	1.704044	3.360463	-2.016144
C	1.677644	2.388515	-1.062358
N	0.539644	1.701083	-1.155132
H	1.118609	4.705201	-4.299797
H	-0.286083	3.676734	-4.707899
H	-1.155428	1.856621	-2.495639
H	2.471724	4.019551	-2.166246
H	2.478062	2.192352	-0.342851
H	-4.976822	-0.343868	-3.696986
C	-4.957871	-0.890719	-2.729729
C	-3.867747	-0.368356	-1.857984

C	-2.591318	-0.817034	-1.548701
N	-3.985680	0.853138	-1.206080
C	-2.830133	1.116072	-0.541920
N	-1.964542	0.124252	-0.746127
H	-4.839523	-1.965177	-2.969068
H	-5.951596	-0.760105	-2.255426
H	-2.082385	-1.743200	-1.828968
H	-4.815303	1.451208	-1.210432
H	-2.655509	2.009122	0.063921
H	-1.392338	5.101356	2.563949
C	-1.565473	4.294686	3.300934
C	-1.185075	2.958439	2.752647
C	-0.686947	2.554929	1.522523
N	-1.329453	1.786102	3.479833
C	-0.943590	0.730389	2.715799
N	-0.552969	1.167835	1.515688
H	-2.641400	4.308178	3.577057
H	-0.987736	4.544648	4.214581
H	-0.418741	3.162843	0.656300
H	-1.672784	1.717661	4.440442
H	-0.962237	-0.315506	3.032596
H	7.238754	-6.659141	5.643474
C	6.157108	-6.885259	5.525104
H	6.004704	-7.295914	4.505557
C	5.223576	-5.681719	5.693646
O	5.095016	-4.879438	4.513270
H	5.903003	-7.679023	6.258380
H	5.531699	-5.057650	6.565602
H	4.194723	-6.039162	5.906475
H	5.982794	-4.554966	4.266810
H	-3.778827	-8.890467	-1.389767
C	-4.469313	-8.200153	-1.919079
H	-5.261915	-8.815503	-2.394160
C	-3.730049	-7.325508	-2.940670
C	-2.623091	-6.430889	-2.389703
C	-2.499524	-6.095859	-1.024551
C	-1.661925	-5.877307	-3.269732
C	-1.450729	-5.287106	-0.547548
C	-0.604654	-5.078212	-2.813330
C	-0.456336	-4.807472	-1.431214
O	0.642595	-4.132630	-1.026965
H	-4.953765	-7.565168	-1.147658
H	-4.476414	-6.688114	-3.470269
H	-3.292846	-7.969573	-3.735431
H	-3.233974	-6.474277	-0.296933

H	-1.733312	-6.098884	-4.348462
H	-1.396058	-5.010385	0.515936
H	0.146432	-4.674793	-3.509036
H	0.793550	-4.189602	-0.034616
H	-4.447519	1.634464	-10.426943
C	-4.265278	2.330570	-9.581231
H	-3.430014	3.000641	-9.876796
C	-4.022266	1.647671	-8.224153
C	-2.803112	0.720864	-8.103998
C	-2.619350	0.234304	-6.656566
N	-1.552975	-0.756217	-6.549109
C	-0.828801	-1.043133	-5.440326
N	-1.034627	-0.371708	-4.285728
N	0.122469	-1.979403	-5.478461
H	-5.172081	2.957922	-9.463841
H	-4.930654	1.068372	-7.944058
H	-3.931236	2.444472	-7.451892
H	-1.877564	1.242253	-8.433036
H	-2.929248	-0.159016	-8.773984
H	-3.582879	-0.184012	-6.280062
H	-2.363818	1.099326	-6.007978
H	-1.420094	-1.379104	-7.348839
H	-0.499467	-0.648065	-3.429858
H	-1.927779	0.093204	-4.130494
H	0.411936	-2.364176	-6.377936
H	0.742361	-2.107758	-4.613631
Fe	0.000000	0.000000	0.000000
C	1.581741	-1.620189	-2.239166
O	0.467963	-1.093710	-1.876914
C	2.829488	-1.588059	-1.362390
O	1.743588	-2.115141	-3.389819
C	2.697220	-1.650538	0.155294
S	1.922933	-0.196221	0.918042
H	3.466143	-2.429644	-1.701536
H	3.711670	-1.710995	0.600629
H	2.151532	-2.550284	0.492607
H	3.370866	-0.658505	-1.650169
C	-0.580306	-1.579225	0.851628
N	-1.005284	-2.516423	1.419100
H	2.022129	-8.514757	2.189180
C	1.067444	-8.063913	1.918226
H	0.460167	-8.757737	1.336914
C	1.277630	-6.795181	1.083914
C	1.981003	-5.626600	1.762102
N	2.891455	-5.927743	2.715100

O	1.732087	-4.449958	1.419144
H	0.517444	-7.827913	2.829226
H	0.305029	-6.408470	0.726548
H	1.861005	-7.022042	0.163557
H	3.478984	-5.222548	3.183421
H	3.075286	-6.901999	2.956046

# 1B

H	-1.339338	4.849709	-3.434678
C	-0.396306	4.298133	-3.639431
C	-0.018305	3.430714	-2.483842
C	-0.336294	2.113787	-2.190715
N	0.715633	3.870022	-1.391049
C	0.825943	2.855093	-0.489726
N	0.181553	1.779904	-0.947856
H	0.382908	5.045060	-3.890358
H	-0.572114	3.680435	-4.541367
H	-0.885971	1.393543	-2.799925
H	1.125646	4.799955	-1.279673
H	1.379481	2.903167	0.452227
H	-3.981117	-1.566730	-4.376808
C	-3.963495	-2.137929	-3.423837
C	-3.226091	-1.347209	-2.397741
C	-1.959275	-1.448496	-1.844784
N	-3.745160	-0.166255	-1.881092
C	-2.821783	0.403169	-1.060213
N	-1.724217	-0.349604	-1.032817
H	-3.499640	-3.119289	-3.642183
H	-5.016211	-2.322563	-3.128735
H	-1.211114	-2.234798	-1.965384
H	-4.674878	0.211963	-2.074655
H	-2.978424	1.335263	-0.512418
H	-3.229539	4.326381	2.433467
C	-3.278643	3.465234	3.126066
C	-2.432151	2.336025	2.628602
C	-1.676069	2.181282	1.474674
N	-2.300578	1.125782	3.295655
C	-1.507399	0.294472	2.560701
N	-1.119227	0.909700	1.448837
H	-4.341309	3.153280	3.210835
H	-2.958231	3.819436	4.127364
H	-1.507588	2.903290	0.672274
H	-2.719010	0.892129	4.198481
H	-1.235593	-0.729725	2.829246

H	-2.951419	0.844964	-10.904774
C	-3.123106	1.516500	-10.037335
H	-2.484316	2.414036	-10.179852
C	-2.856906	0.834654	-8.691252
C	-1.384962	0.505072	-8.409598
C	-1.231538	-0.173897	-7.047126
N	0.168541	-0.355247	-6.668626
C	0.572173	-0.564275	-5.400389
N	-0.345490	-0.676086	-4.413248
N	1.867404	-0.628935	-5.070679
H	-4.180293	1.848759	-10.076682
H	-3.459958	-0.097586	-8.621865
H	-3.227431	1.492592	-7.873457
H	-0.779977	1.437482	-8.419728
H	-0.975357	-0.154465	-9.206752
H	-1.764374	-1.152830	-7.053458
H	-1.716036	0.455508	-6.269207
H	0.870553	-0.411594	-7.409727
H	0.038905	-0.881237	-3.472252
H	-1.277528	-1.032070	-4.623018
H	2.594970	-0.345202	-5.725965
H	2.088119	-0.833880	-4.068536
Fe	0.000000	0.000000	0.000000
O	-0.230965	-1.573681	0.899089
C	1.011456	-0.744375	-1.358243
N	1.628429	-1.125722	-2.290110
H	0.035385	-2.320308	0.309768
H	6.775308	-8.933694	4.803776
C	5.671120	-8.811977	4.836168
H	5.262088	-9.154975	3.863343
C	5.263074	-7.368138	5.123008
O	5.574925	-6.461611	4.054181
H	5.286840	-9.483585	5.631081
H	5.723338	-7.016996	6.075221
H	4.163282	-7.296395	5.252333
H	6.534066	-6.500169	3.873300
H	0.800761	-9.095944	2.132185
C	0.027947	-8.314331	1.975060
H	-0.842333	-8.806079	1.494324
C	0.470409	-7.178108	1.053074
C	1.611475	-6.351421	1.557224
C	2.680677	-6.708247	2.368935
N	1.746431	-5.015634	1.210851
C	2.865186	-4.574049	1.794224
N	3.458211	-5.573750	2.504378

H	-0.292626	-7.956348	2.975376
H	-0.389168	-6.503279	0.863524
H	0.728475	-7.592991	0.051892
H	2.954453	-7.652804	2.847395
H	3.261949	-3.553566	1.728868
H	4.341857	-5.582908	3.056932
H	-5.243912	-7.626514	-0.642509
C	-5.753306	-6.755678	-1.106876
H	-6.753977	-7.093877	-1.448719
C	-4.870549	-6.150864	-2.207707
C	-3.506403	-5.633195	-1.750590
C	-3.218754	-5.263951	-0.418413
C	-2.467132	-5.459160	-2.694199
C	-1.971100	-4.731650	-0.043130
C	-1.216910	-4.933909	-2.335482
C	-0.945636	-4.555437	-0.999365
O	0.251198	-3.975971	-0.714636
H	-5.908519	-6.001331	-0.306963
H	-5.417489	-5.308204	-2.691993
H	-4.708051	-6.893407	-3.018893
H	-3.989741	-5.377178	0.359307
H	-2.641389	-5.752030	-3.743687
H	-1.794647	-4.411444	0.994991
H	-0.417668	-4.806854	-3.081464
H	0.758105	-4.370350	0.107854
C	1.576675	0.425512	0.966892
N	2.535217	0.729347	1.570646

## REFERENCES

1. Griffith, J. S., Theory of E.P.R. in low-spin ferric haemoproteins. *Mol Phys.* **1971**, *21* (1), 135-139.
2. Taylor, C. P. S., The EPR of Low Spin Heme Complexes: relation of the  $t_{2g}$  hole model to the directional properties of the g-tensor and a new method for calculating the ligand field parameters. *Biochim Biophys Acta.* **1977**, *491*, 137-149.
3. Stein, N.; Gumataotao, N.; Hajnas, N.; Wu, R.; Lankathilaka, K. P. W.; Bornscheuer, U. T.; Liu, D.; Fiedler, A. T.; Holz, R. C.; Bennett, B., Multiple States of Nitrile Hydratase from *Rhodococcus equi* TG328-2: Structural and Mechanistic Insights from Electron Paramagnetic Resonance and Density Functional Theory Studies. *Biochemistry* **2017**, *56* (24), 3068-3077.
4. Li, W.; Blaesi, E. J.; Pecore, M. D.; Crowell, J. K.; Pierce, B. S., Second-Sphere Interactions between the C93–Y157 Cross-Link and the Substrate-Bound Fe Site Influence the O<sub>2</sub> Coupling Efficiency in Mouse Cysteine Dioxygenase. *Biochemistry* **2013**, *52* (51), 9104-9119.
5. Solomon, E. I.; Brunold, T. C.; Davis, M. I.; Kemsley, J. N.; Lee, S.-K.; Lehnert, N.; Neese, F.; Skulan, A. J.; Yang, Y.-S.; Zhou, J., Geometric and Electronic Structure/Function Correlations in Non-Heme Iron Enzymes. *Chem Rev.* **2000**, *100* (1), 235-350.
6. Popescu, V.-C.; Münck, E.; Fox, B. G.; Sanakis, Y.; Cummings, J. G.; Turner, I. M.; Nelson, M. J., Mössbauer and EPR Studies of the Photoactivation of Nitrile Hydratase. *Biochemistry* **2001**, *40* (27), 7984-7991.
7. Clay, M. D.; Jenney, F. E.; Hagedoorn, P. L.; George, G. N.; Adams, M. W. W.; Johnson, M. K., Spectroscopic Studies of *Pyrococcus furiosus* Superoxide Reductase: Implications for Active-Site Structures and the Catalytic Mechanism. *J Am Chem Soc.* **2002**, *124* (5), 788-805.
8. Van Doorslaer, S., Continuous wave and pulsed EPR analyses of metalloproteins. In *Electron Paramagnetic Resonance: Volume 21*, The Royal Society of Chemistry: 2008; Vol. 21, pp 162-183.
9. Prisner, T.; Rohrer, M.; MacMillan, F., PULSED EPR SPECTROSCOPY: Biological Applications. *Annu Rev Phys Chem.* **2001**, *52* (1), 279-313.
10. Mims, W. B., Envelope Modulation in Spin-Echo Experiments. *Phys Rev B.* **1972**, *5* (7), 2409-2419.
11. Dikanov, S. A.; Tsvetkov, Y., *Electron Spin Echo Envelope Modulation (ESEEM) Spectroscopy*. Taylor & Francis: 1992.
12. Schweiger, A. J., G., *Principles of Pulse Electron Paramagnetic Resonance*. Oxford University Press: UK, 2001; p 578.
13. Harmer, J.; Mitrikas, G.; Schweiger, A., Advanced Pulse EPR Methods for the Characterization of Metalloproteins. In *High Resolution EPR: Applications to Metalloenzymes and*



*Metals in Medicine*, Berliner, L.; Hanson, G., Eds. Springer New York: New York, NY, 2009; pp 13-61.

14. Dikanov, S. A.; Davydov, R. M.; Gräslund, A.; Bowman, M. K., Two-Dimensional ESEEM Spectroscopy of Nitrogen Hyperfine Couplings in Methemerythrin and Azidomethemerythrin. *J Am Chem Soc.* **1998**, *120* (27), 6797-6805.
15. Hendrich, M. P.; Fox, B. G.; Andersson, K. K.; Debrunner, P. G.; Lipscomb, J. D., Ligation of the diiron site of the hydroxylase component of methane monooxygenase. An electron nuclear double resonance study. *J Biol Chem.* **1992**, *267* (1), 261-269.
16. Bender, C. J.; Rosenzweig, A. C.; Lippard, S. J.; Peisach, J., Nuclear hyperfine coupling of nitrogen in the coordination sphere of the diiron center of methane monooxygenase hydroxylase. *J Biol Chem.* **1994**, *269* (23), 15993-15998.
17. Fischer, A. A.; Miller, J. R.; Jodts, R. J.; Ekanayake, D. M.; Lindeman, S. V.; Brunold, T. C.; Fiedler, A. T., Spectroscopic and Computational Comparisons of Thiolate-Ligated Ferric Nonheme Complexes to Cysteine Dioxygenase: Second-Sphere Effects on Substrate (Analogue) Positioning. *Inorg Chem.* **2019**, *58* (24), 16487-16499.